Title

Origin of enhanced reversible Na ion storage in hard carbon anodes through p-type molecular doping

Journal

Journal of Materials Chemistry A, 10(31)

ISSN

2050-7488

Authors

Lee, Gi-Hyeok
Hwang, Taesoon
Kim, Jae-Bum
et al.

Publication Date

2022-08-10

DOI

10.1039/d2ta02295h

Origin of enhanced reversible Na ion storage in hard carbon anode through p-type molecular doping

Gi-Hyeok Lee,[a,b†] Taesoon Hwang,[c†], Jaebum Kim,[d] Junghoon Yang,[e] Feng Zou,[d] Maenghyo Cho,[*c] Yong-Mook Kang[*d,f]

Na-ion batteries (SIBs) require novel anode materials which have high ion storage capability and low working voltage to make SIBs competitive compared to Li-ion batteries (LIBs). From this perspective, we present the origin of improved electrochemical performances of phosphate doped hard carbon (P-HC) which can meet the two requirements mentioned above through combining experiment with the calculations of atomic/electronic structures. We disclosed that the capacity enhancement is accompanied by the changed voltage profile, which results from the introduced phosphate functional groups. The emerged redox peak turned out to be generated by the electrochemical reaction of Na ions near the phosphate-carbon environment. First-principles calculation elaborated that the phosphate introduction here generates electron holes near the fermi level that is generally considered as evidence of p-type semiconductor to improve electronic conductivity. This expectation has been proven by comparatively measuring the electrical conductivities of pristine hard carbon and P-HC. A close investigation into charge distribution indicated that the electron hole is generated mainly by the higher reducibility of the doped phosphate than the surrounding carbon atoms in P-HC. This discovery well explains the underlying principles for the enhanced electrochemical performance of P-HC. It thereby shows a way to design highly functional hard carbon structures toward higher capacity with Na ions.

Introduction

Na-ion batteries (SIBs) have received significant attention to addressing the price surge of Li caused by the increasing demand for large-scale Li-ion batteries (LIBs). It has been considered as a promising alternative since it has not only a similar operation mechanism to LIBs but also huge and well-dispersed reserves compared to Li finally avoiding the weaponization of resources. However, the anode materials with decent electrochemical performances look essential for the commercialization of SIBs, because graphite, the commercialized anode material for LIBs, is not compatible with SIBs due to the unavailable intercalation with Na ions.[1-3] Among the anode candidates for SIBs, hard carbon has been considered as one of the most balanced anode materials in terms of general electrochemical properties such as working voltage, cyclic stability, reversible capacity and so on.[4, 5] However, the Na-ion storage capacity of hard carbon has been still behind the required capacity to commercialize SIBs by making its performances comparable to those of LIBs. Therefore, improving the capacity of hard carbons looks mandatory to make SIBs a practical replacement for LIBs.[6]

Many previous studies have been typically depending on precise control over surface area or elemental doping to maximize the available capacity of hard carbon.[7-10] However, the enhanced capacities based on these strategies have been typically accompanied by the evolution of the highly sloppy potential region during charge/discharge, making the configuration of full-cells with these hard carbons very difficult. Other than the controlled surface-area and doping strategies, various biomasses have been adopted to control the microstructure of hard carbon toward higher capacities with lower average charge/discharge potentials.[11-16] However, the availability of biomass-derived hard carbon has been limited because of the significant irreversible capacity and the elusive mechanism for the enhanced Na-ion storage.

Recently, several works reported the capacity enhancement in the low potential region by molecular doping into sucrose-based hard carbon.[17-21] Several inorganic acids, including phosphoric acid, were also adopted to tune the microstructure or crystal structure of hard carbon. These works commonly indicated that the phosphates seemingly contribute to increasing the reversible capacity of hard carbon. Thus, combinatory theoretical and experimental analyses have been conducted to determine how the introduced phosphates or phosphorus are associated with enhanced Na-ion storage. However, the model for simulating the mechanism was based on phosphorus-substituted graphene or phosphate-bonded carbon along the basal plane of carbon, which is far away from the actual environment around phosphorus in hard carbon. Therefore, a more reasonable model coupled with experimental validation looks essential to grasp how phosphate contributes to Na-ion storage in hard carbon.

In this work, various aspects of phosphate-doped hard carbon were investigated through various physicochemical and electrochemical analyses, including the chemical bonding of phosphorus in hard carbon. The corresponding information was utilized for a first-principles calculation to identify the electronic structure change of hard carbon through phosphate molecular doping. Considering the chemical similarity between phosphate, nitrate, sulfate, borate, etc., the result of mechanistic study here can be extended to other molecular doping research for hard carbon in the future. Even if some of the aforementioned chemicals have already demonstrated their effect on the electrochemical performances of hard carbon, the corresponding mechanism is still elusive.[17] Therefore, this work may provide a conceptual basis for further research on hard carbon through molecular doping and

thereby enable hard carbon to be an actual anode candidate for NIBs, like graphite anode for LIBs.

Experimental

Preparation of hard carbons

The hard carbons are prepared by sucrose (Sigma-aldrich, 99.5 wt %), graphene oxide solution (GRAPHENEALL, 7 mg mL^{-1}) and phosphoric acid (Duksan, 85 wt %). Three hard carbons named with S-HC, G-HC and P-HC have different components (S-HC: sucrose only; G-HC: sucrose and graphene oxide; P-HC: sucrose, graphene oxide and phosphoric acid). The detailed synthetic procedure was same with the work from Li et al.[20] The mixed components were dried at 80 °C for 48 hr and followed by the dehydration process at 180 °C for 24 hr. The obtained powders were carbonized at 1100 °C for 5hr. The ramp for the carbonization was 4 °C min^{-1}.

Electrochemical measurements

Electrochemical evaluations were performed by preparing hard carbon electrodes using a slurry coating containing the active material (92 wt %), Super P (Timcal; 1 wt %) as a conductive agent, and polyvinylidene fluoride (Kureha KF1100; 7 wt %) as a binder. The resulting slurry was casted onto copper foil and dried in a vacuum oven at 120 °C overnight. After drying, a circular-shaped electrode was punched out. The loading density of the hard carbon electrodes corresponded to ca. 3 mg cm^{-2}. The electrochemical properties of the hard carbons were evaluated using CR2032 coin-type cells assembled in an Ar-filled glove box. Na metal foil was used as a counter and reference electrode. A 1.0 M solution of $NaPF_6$ in EC and DEC (1:1, v/v) was employed as an electrolyte, and 150 µL of electrolyte was added to the coin-type cell. Galvanostatic charge-discharge tests of the coin-type half-cells (*vs.* Na/Na^+) were performed with various cutoff voltages at 10 and 20 mA g^{-1}.

Materials characterization

The FT-IR measurements were carried by ATR mode (Thermo Electron; Nicolet 6700). The ex-situ ^{31}P solid-state MAS NMR measurements were carried with 4mm CP MAS probe spun at 9 kHz. 500 MHz Bruker Avance III HD spectrometer installed at the National Center for Inter-university Research Facilities (NCIRF) at Seoul National University was used for the ex-situ ss MAS NMR analyses. Raman spectra were collected in the 100–3700 cm^{-1} range with a Raman spectrometer (Horiba, NEW XploRA Plus V1.2 Å MULTILINE Confocal Raman microscope) using a 30 mW air cooled laser diode (638 nm, Spectra Physics) and a Olympus MPlanN (10×) magnification objective (0.5 numerical aperture). Spectra were obtained with 25% of the laser beam power and an exposure time of 60 s.

Computation details

To analyze mechanism of this reaction, we examined the atomic and electronic structures based on density functional theory (DFT).[22] In this DFT simulation, we exploit the Vienna Ab Initio Simulation Package (VASP) using the functional of spin-polarized generalized gradient approximation (GGA) parameterized by Perdew-Burke-Ernzerhof (PBE).[23] We construct a modified carbon sheet based on 4x4x1 unit cell of graphene sheet and introduce the plane wave cut-off energy of 500 eV with Monkhorst-Pack setting of 4x4x1 k-point sampling for atomic structures and gamma centered grid of 6x6x1 k-point sampling for electronic structures. In this simulation, we fully relaxed designed structures for thermodynamically stable states by introducing sensitive interaction of van der Waals.[24, 25]

Results and discussions

Correlation between the phosphate doping and Na ion storage

To investigate the effect of phosphate, we prepared phosphate-doped hard carbon as reported in the previous work.[20] The hard carbons in this work were prepared with the combination of sucrose, graphene oxide (GO), and phosphoric acid (PA). S-HC is prepared with only sucrose, G-HC is prepared with sucrose and GO, and P-HC is prepared with sucrose (5 g), GO (62.5 mg), and PA (0.25 g). The detailed synthetic procedure was described in experimental details.

Figure 1 shows the electrochemical properties of phosphate-doped hard carbon (P-HC). As the standard hard carbon (P-HC) is made of various precursors, sucrose, GO, and PA, we prepared hard carbons having different concentrations of components to separate the contribution from GO and phosphoric acid (PA) to the capacity increase. The colored parts of insets in Figure 1a and 1b indicate which parameters are varied.

Figure 1a compares voltage profiles of hard carbons when the concentration of GO in hard carbon was varied without change of contents of PA. When increasing the contents of GO, the first discharge capacity was increased, and a redox shoulder at ~0.5 V emerged. However, those two capacities were not reflected in the first charging process, which means that the changes due to the GO increment were not reversible and may be induced by the SEI formation. On the other hand, the first discharge capacity and the plateau at ~0.5 V were decreased. Interestingly, the redox shoulder was clearly observed during the charging process, suggesting less relevance between the shoulder and GO contents variation.

Figure 1b shows the results from the opposite case; the amount of PA was varied without a change of GO contents. The hard carbon having higher contents of PA showed the decreased first discharge capacity and no apparent change in the redox shoulder. However, the shoulder looks much enhanced during

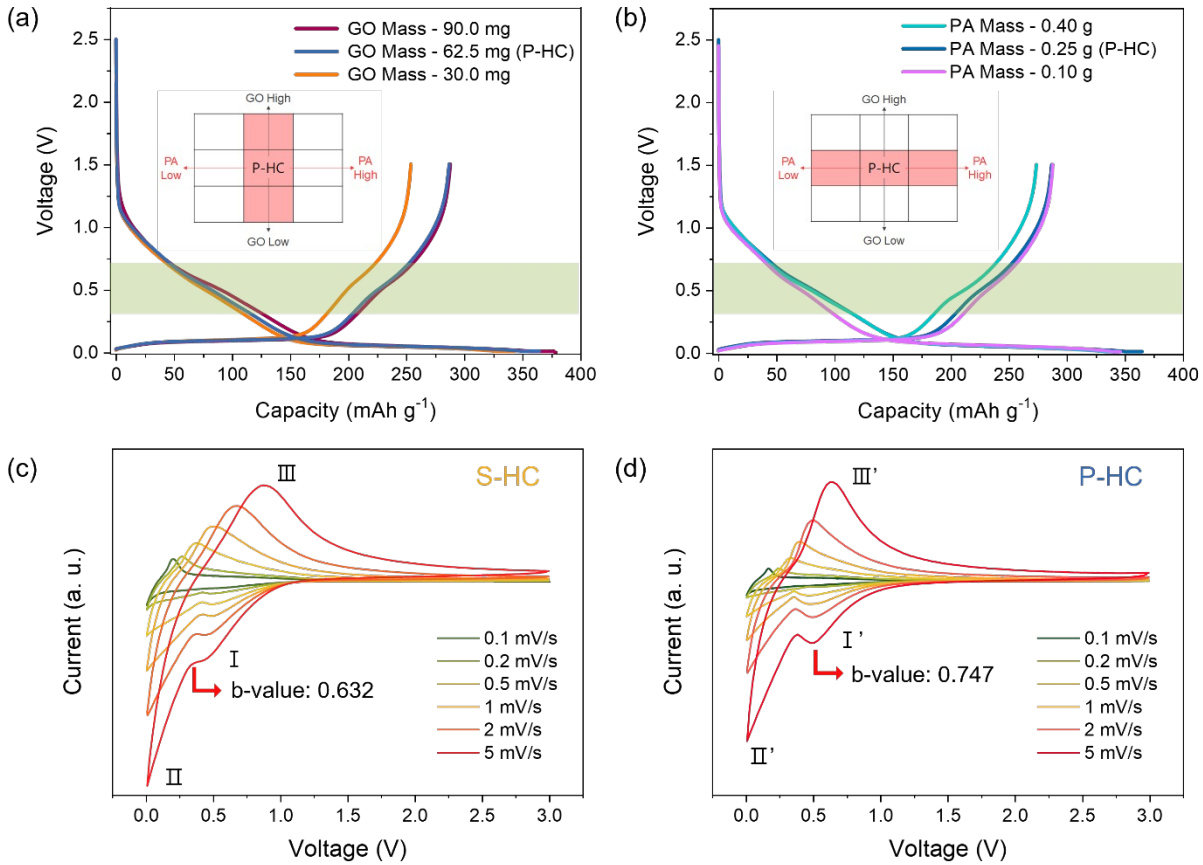

Figure 1. Comparison of initial voltage profiles of P-HCs which have different concentration of (a) graphene oxide (GO) and (b) H_3PO_4 (PA). The insets illustrate the which hard carbon component is variable or constant. The cyclic voltammetry of (c) S-HC and (d) P-HC in various scan speeds.

the first charging process. When it comes to the hard carbon having decreased contents of PA, it showed better first coulombic efficiency and the weakened shoulder. The capacity of hard carbon without PA (G-HC) was also investigated to check the capacity enhancement by the PA (**Figure S1**).

As suggested in the comparisons, the most distinct changes of the voltage profiles are the capacities and the change of intensity of the redox shoulder highlighted with green boxes in Figures 1a and 1b. The intensity of the shoulder was changed when the amount of PA was controlled, while no change occurred when GO contents was controlled. It implies that the PA directly contributes to the reduction peak at ~0.5 V.

The cyclic voltammetry (CV) curves of S-HC and P-HC were shown in Figure 1c and 1d show the change of reduction peak more clearly. The S-HC shows a relatively more minor reduction shoulder at ~0.5 V (Peak I) and sharp redox peak (Peak II) at the low potential region, and P-HC show a more developed ~0.5 V peak (Peak I') and broadened low potential reduction peak (Peak II'). Moreover, the b-values calculated from the peak I and I' show that the electron exchange process is more pseudo capacitive after phosphate doping. Unfortunately, the b-value calculations for other peaks (II, II', III, and III') are unavailable because the background extraction for those peaks is impossible. However, the degree of the peak shift for III and III' towards high-voltage implies the oxidation process of hard carbon is also more pseudocapacitive. Therefore, both reduction peak in P-HC was seemingly affected by the phosphate doping and being more pseudocapacitive, the additional capacities arose from pseudocapacitive interactions.

Chemical structure deduction of the phosphate-neighbouring sites

To clarify the redox contribution of the phosphate functional group, verifications of the chemical structure of the phosphate in P-HC are essential. The Fourier transformed-infrared (FT-IR) spectroscopy and ^{31}P solid-state NMR (ssNMR) analyses have been employed to get chemical information of hard carbon.

Figure 2a compares the FT-IR spectra of three hard carbons consisted of different components. The yellow, green, and blue solid lines indicate S-HC, G-HC, and P-HC, respectively. The dotted lines indicate new peaks for functional groups occurred by new components added to pure sucrose-based hard carbon. The peak from the hydroxyl group (-OH; located at ~3500 cm^{-1}) was increased after rGO was adopted because rGO has many hydroxyl groups on their basal plane.[26] Also, a peak near 1250 cm^{-1} was increased after the addition of PA. The peak corresponds to P=O bonds, and Figure 2b supports proving the peak is from P=O bonds.[27, 28] As the P=O peak is located very close to another strong peak at ~1100 cm^{-1}, we tried to crosscheck the peak by controlling the concentration of PA. As the intensity ratio of the peak from P=O bond to the peak at ~1100 cm^{-1} increases as the concentration of PA is increased, we could deduce this peak occurs from P=O bonds.

Figure 2. FT-IR results of (a) hard carbons consisted of different components and (b) hard carbons made of different concentration of PA.

The ^{31}P solid-state magic angle spinning nuclear magnetic resonance (ss-MAS NMR) spectroscopy can provide another clue for the structure of phosphorus compounds, and it is suggested in **Figure 3**. Based on the chemical shift of phosphorus, we could narrow down the candidates of the structure with the negative chemical shift as the pristine P-HC shows. The analogies of $O=P(OR)_3$ are also considered as the most reliable structures satisfying both the negative chemical shift and the P=O bond (known from the FT-IR).[29] Even though the PA molecule (H_3PO_4) also can be one of the possible candidates for the condition, it is more reasonable that the phosphorous compound is chemically bound to the alkyl group considering the boiling point of PA (158 °C) is much lower than the carbonization temperature (1100 °C). One plausible scenario is that, as the sucrose, which is a precursor of hard carbons, has many -OH functional groups, the facile esterification between PA and -OH group is possible between 160 to 250 °C and could make a chemical bonding as following chemical equation. The dehydration process of the P-HC is conducted under 180 °C, the esterification reaction like **Equation 1** can occur during the process.

$$ROH + H_3PO_4 \rightarrow ROPO_3H_2 + H_2O \quad (1)$$

The other scenario is the dimerization of phosphate at a high temperature over 400 °C. However, the reaction seems hard to happen because the temperature for the dimerization is too high to confine the vaporized PA near the functional group. Furthermore, the chemical shift of ^{31}P ssNMR does not match with polyphosphates.[29]

In addition, Raman spectroscopy was employed to check the structural evolution of the hard carbon after adding additional precursors such as GO and PA. As shown in the Figure S2, the Raman spectra of the samples showed a negligible change. The I_D/I_G ratio which indicates the degree of misalignment of graphitic structure slightly increases as the number of precursors increases, presumably due to the local alignment distortion around the additional precursors.

To clarify the underlying mechanism of the phosphate for Na-ion storage, we formulated an approximate model of phosphate functionalized graphene layers (P-GL) in P-HC in **Figure 4** for the DFT calculation based on the results from FT-IR and ssNMR. The model represents the local structure where the phosphates are engaged. Therefore, the calculated properties from the model leverage the understanding of the role of phosphates. Figure 4a shows the total density of states (TDOS) of graphene layers (GL) and P-GL, and new energy states (highlighted with orange dotted boxes) in TDOS of P-GL are observed near the Fermi level, while the states are not found in the GL. In addition, the spatial distribution shown in Figure 4b-c and 4e-f of unoccupied electron energy states from 0 eV to 1 eV of P-GL is larger than GL, it means that the energy states near the Fermi level was generated in P-GL and the spatial distribution results correspond to newly generated energy states of TDOS. The new energy states near Fermi level are usually observed in p-type conductivity, which implies that

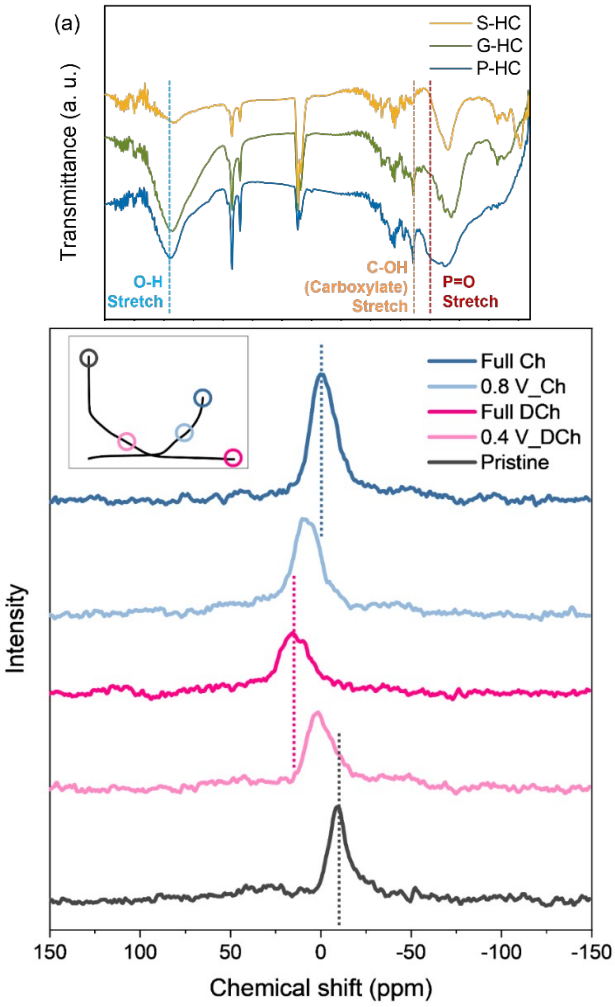

the PA functionalization of HC could be sorted as p-type doping.[15] These hole states are known as making electrons to being easily transferred into the P-HC environment. Particularly, the occurrence of electronic hole states for P-HC could generate an empty energy level used as a highly activated electron acceptor considering that the electron

Figure 3. Ex-situ ^{31}P MAS NMR experiment results of P-HC.

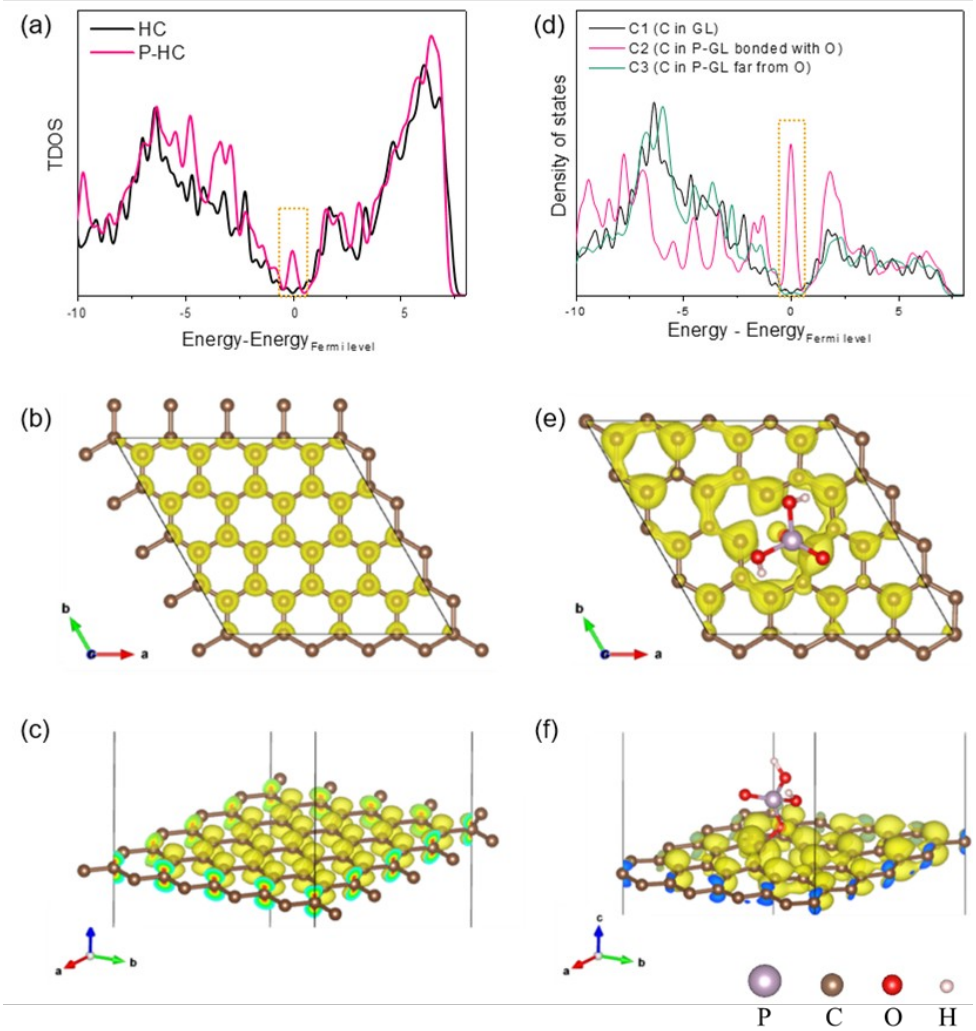

Figure 4. Calculated (a) total density of states (TDOS) and (b) projected density of states (PDOS) of graphene layers. Spatial electron distribution of the unoccupied states from fermi level from 0 eV to 1 eV of (b-c) GL and (e-f) P-GL.

transferring reaction occurs near the Fermi level. Therefore, this tuned electronic structure would thermodynamically facilitate binding between Na-ion and P-HC. To validate the p-type conductivity of P-HC, the electronic conductivities of hard carbons were measured by powder resistivity measurement system as shown in **Table S1**. The electronic conductivities of S-HC, G-HC, and P-HC were compared to single out the effect of phosphate dopant, and they showed about 24, 35, and 40 S cm^{-1} of electric conductivity, respectively. The values are averaged by three repetitive measurements, and the errors are negligible. The increase of electric conductivity from 24 to 35 S cm^{-1} is attributed to the reduced graphene oxide. Therefore, the increase of 35 to 40 S cm^{-1} is supposed to arise from the doping of phosphate in the hard carbon as shown in the case of P-GL. Considering the phosphate compounds usually have lower electronic conductivity than carbonaceous materials, the simple composite of phosphates and carbonaceous materials without the modification of electronic structure is expected to show lower electric conductivity. Thus, the increase of electric conductivity of P-HC implies that the modification of the electronic structure of hard carbons by phosphate doping. In addition, the hole generation is known to enhance the electronic kinetics of electrodes and then improve the rate capability.[30] Table S1 shows that P-HC has the higher electronic conductivity than S-HC and it is consistent with the result that p-type conductivity from the hole generation increases the electronic kinetics. The kinetics enhancement is also reflected in the cyclic voltammetry comparison between S-HC and P-HC

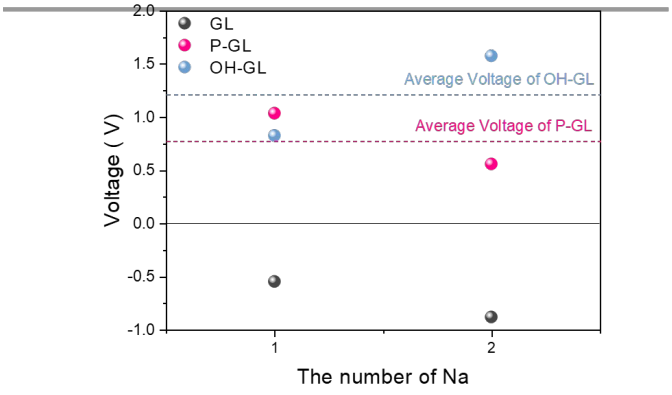

Figure 5. Calculated average voltages of hard carbons.

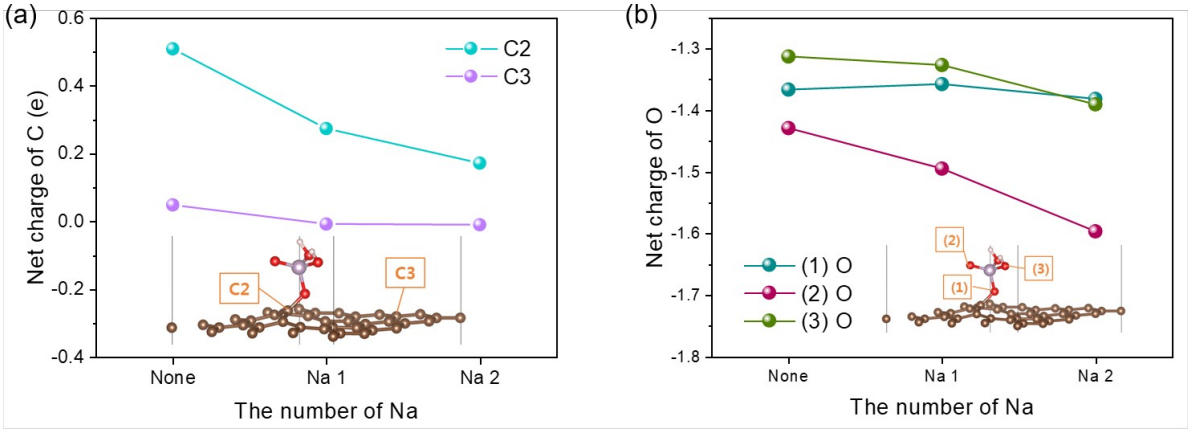

Figure 6. Average net charges variation of (a) carbons and (b) oxygens according to the Na-ion contents.

(Figure 1c and d), which shows a relative relief of polarization for the P-HC.

To clarify the origin of this p-type conductivity in P-HC, we also investigated the projected density of state (PDOS) of carbon in GL and P-GL, as shown in Figure 4b. Figure 4b exhibits that the carbon bonded with O of phosphate (C2) has been tuned to having hole states in the vicinity of Fermi level, while the carbon far from O (C3) in P-GL has similar energy states with carbon's energy states in GL (C1). According to these PDOS, the origin of p-type conductivity by the hole generation arose from the carbon bonded with the phosphate group.

Na-ion storage mechanism of phosphate-neighboring structure

To investigate the contribution of phosphate to the sodiation process, ex-situ solid-state ^{31}P MAS NMR spectroscopy and DFT calculation. First, we simulated the Na ion insertion of phosphorous-neighboring structure in hard carbon by using the structural model of Figure 4. The sodiation voltages of GL with -OH functionalized graphene layer (OH-GL) and P-GL representing the P-HC were calculated to explain the change of the carbon environment when the phosphorous compound was doped in different Na-ion concentrations (**Figure S3**). Unlike other alkali-ions of Li and K, Na-ion is known as being intrinsically difficult to bind with graphitic layer by transferring electrons thermodynamically.[9, 31, 32] **Figure 5** shows how the functionalization modifies the thermodynamic character of the graphene layer. The average voltages (V_{avg}) of the sodiation are ~ -0.75 V of GL, ~1.25 V of OH-GL and ~0.75 V of P-GL as calculated by $V_{avg} = \frac{1}{n}[E_{total}(Na_{1-n}X\text{-GL}) + (n\text{-}1)E_{total}(Na) - E_{total}(Na_nX\text{-GL})]$ where X are the functionalized states (i.e., no introduction of OH and P) and n is the number of Na-ions. The calculated average voltage of OH-GL is relatively high comparing with P-GL and this tendency also corresponds to the newly generated redox peak discrepancy between G-HC retaining many -OH groups and P-HC in Figure 1 and 2. As the positive average voltage suggests the reaction is thermodynamically stable, it means that the carbon layers with defects and functional groups are thermodynamically tuned to easily accept the Na-ion, while the negative voltage of GL indicates the binding between GL and Na-ion is thermodynamically unstable.[16, 17, 33] However, the reaction voltage of sodiation in OH-GL increases when another Na-ion is inserted. It implies the Na-ion strongly bonds with OH-GL and can be trapped in the site irreversibly. Therefore, the application of PA can increase the reversible Na-ion storage considering the redox potential ranges.

To investigate the detailed Na-ion storage sites of the structures, net charge analyses for the carbon and oxygen were conducted. Considering the carbons in graphitic anode materials being used as the main redox center, we examined the redox mechanism by analyzing the charge variation of these carbons as Na-ion contents. **Figure 6a** indicates the net charges of C2 and C3 in P-GL. Interestingly, the electron is mainly accumulated in the C2, not the C3 that has similar intrinsic electronic properties of carbon on HC. When the Na-ion is inserted in P-HC, the net charge of C2 is more negatively changed than C3. In addition, the generated hole energy states of C2 get reduced as the concentration of Na-ion increases as shown in **Figure S4**. Considering the redox mechanism, we could deduce that carbon of P-GL was tuned to retaining new intrinsic property and facilitate the reaction with Na-ion as redox center of anode material for SIBs by adopting PA, while conventionally considered carbonaceous materials undergo difficulties of electrochemical interaction with Na-ion.

In addition, the O1, O2 and O3 of phosphate also indicate charge variation and O2 shows the highest variation that represents more than twice variations of O1 and O3. Then, we could relate this charge variations of redox centers (C2, O2) and voltage regions, even if the ratio of accepting electron to O2 of 0.17 e^- (Figure 6b) is much lower than the charge variation of the modified carbon (C2) of 0.34 e^- (Figure 6a) after addition of PA during the sodiation. The calculated voltages range could be divided into two regions of relatively high (one Na-ion reaction) and low (two Na-ion reaction) voltages. Comparing with charge variations of redox centers, C2 undergoes more charge variation of 0.24 e^- in high voltage than 0.1 e^- in low voltage. On the other hand, O2 accept more electrons of 0.1 e^- in low voltage than the electron gathering of 0.07 e^- in high voltage. Based on the charge variation of redox centers in two calculated voltage regions, the charge of P-GL varies at C2 as the major redox center during all the sodiation regions. In addition, these accepted electrons by the redox

centers are confirmed from the spatial electron distributions from 0 eV to -1 eV (**Figure S5**). Figure S5 indicates the electrons are mainly accumulated near the redox centers.

The ex-situ NMR results validate the results from the theoretical calculations. The chemical shift changes of ssNMR spectra during the charge/discharge process suggest that the (de)sodiation process affects the electron density near the phosphorus atom. The inset indicates the points where the ex-situ analyses were conducted. As shown in Figure 3, when the Na-ions are inserted during the discharging process, the peak is located more downfield during discharging and shifted upfield again after the charging process was finished. In NMR, however, the downfield of the chemical shift indicates the decrease of electron density near the target atom. Therefore, the electron density near the phosphorus is decreased after the sodiation. At first glance, it looks conflict with the increase of electron density near the oxygen in the phosphate. However, the spatial charge density variation shown in Figure S6 well explains the electron density changes in the phosphate after the sodiation. Figure S6 exhibits that the electron charge density between phosphorus and oxygen decreased during the sodiation, which is consistent with the results from ex-situ NMR. In addition, we also confirmed that these decreases in electron charge densities verified with and a variation on the bond length of P=O, as shown in Table S2 The bond length of P=O bond increases depending on the amount of Na-ion near the phosphate. As referred above, an increase of P=O bond length indicates the decrease of electron density between P and O. It is noteworthy that the chemical shift of phosphorus kept shifted downfield over the 0.5 V discharge, which means the phosphorus compound contribute through the low voltage sodiation process of P-HC, which is consistent with the broadening of peak II' even though we could not separate the contribution of PA from peak II. Also, it is consistent with the results from Figure 6, which expected the contribution of phosphate at low voltage Na insertion.

Conclusions

We have investigated the contribution of PA introduction to sodiation and desodiation of hard carbon by experimental and theoretical aspects. The FT-IR and ssNMR gave an insight for the plausible chemical structure of phosphate neighboring sites. The DFT calculation based on the reasonably designed model supports the experimental results and explains the origin of Na-ion storage capability. The additional sodiation of P-HC was achieved by the occurrence of p-type conductivity in the carbon layer by PA doping and the co-contribution of carbon and oxygen. The phosphate group has better reversibility of Na-ion storage than other functional groups such as -OH. Our results provide a reasonable solution to understand the elusive molecular doping effect of carbon materials, and we expect the finding will be helpful to understand and design high-capacity carbonaceous materials.

Author Contributions

Gi-Hyeok Lee: Conceptualization, Formal analysis, Writing - Original draft **Taesoon Hwang:** Methodology, Writing – Original draft **Jaebum Kim:** Validation, Formal analysis **Junghoon Yang:** Investigation **Feng Zou:** Validation **Maenghyo Cho:** Funding acquisition, Supervision **Yong-Mook Kang:** Supervision, Funding acquisition, Writing – Review & Editing

Conflicts of interest

There are no conflicts to declare.

Acknowledgements

Y.-M.K. acknowledges the support of this research by National Research Foundation of Korea (NRF) grants funded by the Korean government (MSIP; NRF-2017R1A2B3004383). G.-H.L. acknowledge the financial support of the ALS fellowship program. M. Cho acknowledges The National Research Foundation of Korea (NRF) grant funded by the Korea government (MEST) (2012R1A3A2048841).

References

1 N. Yabuuchi, K. Kubota, M. Dahbi and S. Komaba, *Chem. Rev.*, 2014, **114**, 11636.
2 X. Xiang, K. Zhang and J. Chen, *Adv. Mater.*, 2015, **27**, 5343.
3 D. A. Stevens and J. R. Dahn, *J. Electrochem. Soc.*, 2000, **147**, 1271.
4 Y. Cao, L. Xiao, M. L. Sushko, W. Wang, B. Schwenzer, J. Xiao, Z. Nie, L. V. Saraf, Z. Yang and J. Liu, *Nano Lett.*, 2012, **12**, 3783.
5 E. Irisarri, A. Ponrouch and M. R. Palacin, *J. Electrochem. Soc.*, 2015, **162**, A2476.
6 K. M. Abraham, *ACS Energy Lett.*, 2020, **5**, 3544.
7 A. Agrawal, K. Biswas, S. K. Srivastava and S. Ghosh, *J. Solid State Electrochem.*, 2018, **22**, 3443.
8 Q. Huang, J. Hu, S. Wen, X. Zhang, G. Liu, S. Chang and Y. Liu, *Front. Chem.*, 2020, **8**, 241.
9 Q. Jin, K. Wang, P. Feng, Z. Zhang, S. Cheng and K. Jiang, *Energy Storage Mater.*, 2020, **27**, 43.
10 Y. Wang, Y. Li, S. S. Mao, D. Ye, W. Liu, R. Guo, Z. Feng, J. Kong and J. Xie, *Sustain. Energy Fuels*, 2019, **3**, 717.
11 P. Liu, Y. Li, Y.-S. Hu, H. Li, L. Chen and X. Huang, *J. Mater. Chem. A*, 2016, **4**, 13046.
12 J. Górka, C. Vix-Guterl and C. Matei Ghimbeu, *C*, 2016, **2**, 24.
13 T. K. Kumaresan, S. A. Masilamani, K. Raman, S. Z. Karazhanov and R. Subashchandrabose, *Electrochim. Acta*, 2021, **368**, 137574.
14 X. Ren, S.-D. Xu, S. Liu, L. Chen, D. Zhang and L. Qiu, *J. Electroanal. Chem.*, 2019, **841**, 63.
15 K.-l. Hong, L. Qie, R. Zeng, Z.-q. Yi, W. Zhang, D. Wang, W. Yin, C. Wu, Q.-j. Fan, W.-x. Zhang and Y.-h. Huang, *J. Mater. Chem. A*, 2014, **2**, 12733.
16 Y. Li, S. Xu, X. Wu, J. Yu, Y. Wang, Y.-S. Hu, H. Li, L. Chen and X. Huang, *J. Mater. Chem. A*, 2015, **3**, 71.
17 Z. Li, C. Bommier, Z. S. Chong, Z. Jian, T. W. Surta, X. Wang, Z. Xing, J. C. Neuefeind, W. F. Stickle, M. Dolgos, P.

A. Greaney and X. Ji, *Adv. Energy Mater.*, 2017, **7**, 1602894.
18 S. Alvin, C. Chandra and J. Kim, *Chem. Eng. J.*, 2020, **391**, 123576.
19 F. Wu, R. Dong, Y. Bai, Y. Li, G. Chen, Z. Wang and C. Wu, *ACS Appl. Mater. Interfaces*, 2018, **10**, 21335.
20 Z. Li, L. Ma, T. W. Surta, C. Bommier, Z. Jian, Z. Xing, W. F. Stickle, M. Dolgos, K. Amine, J. Lu, T. Wu and X. Ji, *ACS Energy Lett.*, 2016, **1**, 395.
21 Y. Jin, S. Sun, M. Ou, Y. Liu, C. Fan, X. Sun, J. Peng, Y. Li, Y. Qiu, P. Wei, Z. Deng, Y. Xu, J. Han and Y. Huang, *ACS Appl. Energy Mater.*, 2018, DOI: 10.1021/acsaem.8b00354, 2295.
22 G. Kresse and J. Furthmüller, *Comput. Mater. Sci*, 1996, **6**, 15.
23 J. P. Perdew, K. Burke and M. Ernzerhof, *Phys. Rev. Lett.*, 1996, **77**, 3865.
24 G. Yoon, D.-H. Seo, K. Ku, J. Kim, S. Jeon and K. Kang, *Chem. Mater.*, 2015, **27**, 2067.
25 Y.-J. Kang, S. C. Jung, J. W. Choi and Y.-K. Han, *Chem. Mater.*, 2015, **27**, 5402.
26 R. B. Church, K. Hu, G. Magnacca and M. Cerruti, *J. Phys. Chem. C*, 2016, **120**, 23207.
27 P. Y. Shih, S. W. Yung and T. S. Chin, *J Non Cryst, Solids*, 1999, **244**, 211.
28 A. Majjane, A. Chahine, M. Et-tabirou, B. Echchahed, T.-O. Do and P. M. Breen, *Mater. Chemi. Phys.*, 2014, **143**, 779.
29 A. Zheng, S.-B. Liu and F. Deng, *Chem.l Rev.*, 2017, **117**, 12475.
30 T. Hwang, J. M. Lim, R. G. Oh, W. Cho, M. Cho and K. Cho, *Phys. Chem. Chem. Phys.*, 2021, **23**, 5438.
31 V. Palomares, P. Serras, I. Villaluenga, K. B. Hueso, J. Carretero-González and T. Rojo, *Energy Environ. Sci.*, 2012, **5**, 5884.
32 H. Wang, F. Sun, Z. Qu, K. Wang, L. Wang, X. Pi, J. Gao and G. Zhao, *ACS Sustain. Chem. Eng.*, 2019, **7**, 18554.
33 H. Xie, Z. Wu, Z. Wang, N. Qin, Y. Li, Y. Cao and Z. Lu, *J. Mater. Chem. A*, 2020, **8**, 3606.